Author Contributions:
Conceptualization: Rocio Jaimes-Gutierrez, Thierry Adatte, Sebastien Castelltort
Formal analysis: Rocio Jaimes-Gutierrez, Thierry Adatte, Emmanuelle Pucéat, Torsten Vennemann, Sebastien Castelltort
Funding acquisition: Sebastien Castelltort
Methodology: Rocio Jaimes-Gutierrez, Thierry Adatte, Torsten Vennemann

Deciphering Paleocene-Eocene Thermal Maximum Climatic Dynamics: Insights From Oxygen and Hydrogen Isotopes in Clay Minerals of Paleosols From the Southern Pyrenees

Rocio Jaimes-Gutierrez[1] , Thierry Adatte[2], Emmanuelle Pucéat[3] , Torsten Vennemann[4] , Marine Prieur[1] , Amanda L. Wild[5], Hassan Khozyem[6], Romain Vaucher[1,2] , and Sebastien Castelltort[1]

[1]Department of Earth Sciences, University of Geneva, Geneva, Switzerland, [2]Institute of Earth Sciences, Géopolis, University of Lausanne, Lausanne, Switzerland, [3]Biogéosciences, UMR 6282, UBFC/CNRS, Université Bourgogne Franche-Comté, Dijon, France, [4]Institute of Earth Surface Dynamics, Géopolis, University of Lausanne, Lausanne, Switzerland, [5]Helmholtz Center Potsdam, GFZ German Research Center for Geosciences Institute of Earth and Environmental Science, Universität Potsdam, Potsdam, Germany, [6]Geology Department, Faculty of Science, Aswan University, Aswan, Egypt

Abstract This study focuses on the Paleocene-Eocene Thermal Maximum (PETM), a hyperthermal event characterized by a rapid increase in global temperature (5–8°C) over 20 ka, in the Southern Pyrenean Foreland Basin. Although there is evidence of increased flood discharge and erosion in the Southern Pyrenees, how paleoclimatic conditions and weathering evolved remains to be assessed. This study focuses on the catchment scale climatological changes recorded in the clay minerals of floodplain paleosols, giving insights into how rainfall affected the weathering regime during and after the hyperthermal event. The oxygen ($\delta^{18}O$) and hydrogen (δD) isotope compositions were analyzed in two clay fractions in paleosols of the Esplugafreda continental section. The clay minerals comprise a dominant smectite-rich assemblage, which indicates a predominantly seasonal, semi-arid climate throughout the section. Two positive excursions in the $\delta^{18}O$ record during the Pre-Onset Excursion (POE) and the Syn-PETM support an increase in air near-surface temperature. Using the δD and $\delta^{18}O$ smectite fractionation factors, we estimate a Mean Annual Air Temperature (MAAT) of $24.2 \pm 1.0°C$ for the POE and $27.0 \pm 0.8°C$ for the Syn-PETM. The δD values show a relatively stable composition during the climatic disturbance, which suggests that this mid-latitude catchment was overall characterized by low yearly rainfall, with a peak in extreme events during the body of the PETM and a trend toward aridification during the recovery phase of the PETM, supported by the paleosol morphotype. These climatic conditions suggest a kinetically controlled weathering regime, where physical transport of the sediments played a primary role as a denudation mechanism.

Plain Language Summary We investigate the Paleocene-Eocene Thermal Maximum (PETM), a global warming event occurring 56 million years ago, and its local impact on the Spanish Pyrenees' climate. During the PETM, global temperatures rose by 5–8°C, prompting us to examine its influence on local mean annual temperature and precipitation. To understand how mountain rocks underwent physical and chemical breakdown into smaller, compositionally different minerals (weathering), we aim to unravel the processes of local climatic change during the PETM. Our study presents the hydrogen and oxygen isotopic composition of clay minerals in river floodplains, reflecting the climate in which they formed. A rise in heavy oxygen isotopes is observed before and during the PETM, confirming higher temperatures in the region by ~3°C. However, hydrogen isotope composition remained unchanged, indicating minimal variations in annual rainfall. Although overall yearly precipitation may have remained steady, the PETM led to infrequent but extreme rainfall events. The precipitation variability implies that erosion played a significant role in the rock-wasting process, making weathering efficiency the limiting factor in forming secondary clay minerals.

1. Introduction

Reconstructing temperature variability and precipitation amount and distribution throughout the year is critical to understanding the implications of climate change for the denudational regime (e.g., García-García et al., 2023; Gariano & Guzzetti, 2016; Haque et al., 2019; Herman et al., 2013; Molnar & England, 1990; Trenberth et al., 2003). While regular, moderate rainfall enhances soil infiltration and promotes plant growth, precipitation

concentrated in extreme rainfall events can lead to enhanced overland runoff, flooding, and even landslides, impacting landscape evolution (Gariano & Guzzetti, 2016; Haque et al., 2019; Trenberth et al., 2003). Soil temperature and moisture impact the soil's heat budget, resulting in critical feedback with air temperature (Burgener et al., 2016; Gallagher & Sheldon, 2016; Gallagher et al., 2019; García-García et al., 2023; Kelson et al., 2020, 2023; Peters et al., 2013; Tabor et al., 2013). With global warming, the Clausius-Clapeyron equations indicate that a rise of 1°C increases the water-holding capacity of the atmosphere by 7% (Coumou & Rahmstorf, 2012; Held & Soden, 2006), likely enhancing the occurrence of extreme precipitation events and the entire hydrological cycle proportionally if a moisture supply is available (Carmichael et al., 2018; Huntington, 2010; Pratap & Markonis, 2022; Rush et al., 2021). Yet the evolution of rainfall distribution and extreme precipitation events with global warming remains unclear (e.g., Coumou & Rahmstorf, 2012; Donat et al., 2017; Edenhofer et al., 2014).

1.1. The Paleocene-Eocene Thermal Maximum

The isotopic composition of hydrogen (δD) and oxygen (δ^{18}O) can be used to trace processes influencing air temperature, soil temperature, and rainout effect in modern and ancient environments (e.g., Bauer et al., 2016; Grujic et al., 2018; Rosenau & Tabor, 2013; Sheppard & Gilg, 1996). Extreme warming events in the geological record, like the Paleocene-Eocene Thermal Maximum (PETM), can provide insights into the response of the hydrological cycle and landscape evolution to extreme climate warming. The PETM was a greenhouse-gas-induced hyperthermal warming event occurring 56 Ma ago (e.g., Bralower et al., 2018; Charles et al., 2011; Kennett & Stott, 1991; Thomas & Shackleton, 1996; Zachos et al., 2003, 2005). The PETM is identified at the global scale by a negative carbon isotope excursion (CIE) of 3–5‰ resulting from a massive release of isotopically light carbon (Dickens et al., 1995; Kennett & Stott, 1991; Wright & Schaller, 2013; Zachos et al., 2005). The CIE is presumed to have had a rapid onset (4–20 ka) (e.g., Kirtland Turner et al., 2017; Lyons et al., 2019), followed by a 70–100 ka long phase of characteristic stable but anomalous low carbon isotopic composition (δ^{13}C) values ("body" of the PETM) (e.g., Zeebe & Lourens, 2019) and a final "recovery" phase of 50–100 ka duration (e.g., Bowen & Zachos, 2010; Cui et al., 2011; Röhl et al., 2007; Westerhold et al., 2017). The PETM is associated with ocean acidification and changes in the ocean circulation pattern (e.g., Penman et al., 2014; Westerhold et al., 2009; Zachos et al., 2003, 2005).

On land, the PETM resulted in significant hydrological changes (Carmichael et al., 2017, 2018; Chen et al., 2018; B. Z. Foreman, 2014; Foreman et al., 2012; Prieur et al., 2024; Pujalte et al., 2015, 2016; Schmitz & Pujalte, 2007; Vimpere et al., 2023), northward migration of plants in North America (e.g., Wing & Currano, 2013), and mammalian biogeographic reorganization (e.g., Clyde & Gingerich, 1998). An increase in kaolinite influx in clay mineralogical assemblages was recorded in several marine sections, for example, on the Bay of Biscay (Bolle & Adatte, 2001; Bolle et al., 2000; Schmitz et al., 2001), the Eastern coast of North America (John et al., 2012), the Antarctic offshore (Robert & Kennett, 1992), the Eastern North Atlantic (Bornemann et al., 2014), and Svalbard (Dypvik et al., 2011). This kaolinite peak has been interpreted as increased physical erosion of previously formed sediments (John et al., 2012; Pujalte et al., 2015). In addition, simulations based on coupled atmosphere-ocean models subject to greenhouse forcing with Paleocene-Eocene paleogeography show a decoupling between the mean and extreme distribution of precipitation in different regions of the world (Carmichael et al., 2018). This decoupling raises the question of how the absolute amount of annual rainfall (Mean Annual Precipitation, MAP) and its frequency-intensity distribution evolved with the climatic perturbation.

The PETM is well recorded in the Southern Pyrenees, where the sedimentary archives suggest a significant change in the hydrological cycle (Baceta et al., 2011; Chen et al., 2018; Colombera et al., 2017; Prieur et al., 2024; Pujalte et al., 2015, 2016; Schmitz & Pujalte, 2007). Detrital sediment accumulation rates in the paleo Bay of Biscay increased more than 4-fold (Dunkley Jones et al., 2018) with increase in yearly water discharge in the Southern Pyrenees during the early phase of the PETM (Chen et al., 2018). In the continental realm, changes in paleosol coloration, presence and distribution of soil nodules, and calcite content have been suggested to record a semi-arid climate with low soil moisture during the PETM (Basilici et al., 2022; Dreyer, 1993; Schmitz & Pujalte, 2007). The Claret Conglomerate, deposited at the onset of the PETM, has been interpreted as the inception and development of a mega fan associated with the abrupt change in seasonality with extreme rainfall events (Baceta et al., 2011; Schmitz & Pujalte, 2003, 2007; Schmitz et al., 2001). Paleohydrological reconstructions later suggested an increase of volumetric peak channel-forming discharge during the early PETM (Chen et al., 2018), a number higher but not inconsistent with the CAM5 (Community Atmosphere Model,

version 5.3) modeled prediction of a 2.79-fold increase in MAP in the Southern Pyrenees by Rush et al. (2021) during the PETM. Based on palynofloral climate reconstructions, hot, dry summers and mild, wet winters with episodic rains throughout the year characterized the southern Pyrenean climate (Korasidis et al., 2022). Climate modeling suggests atmospheric rivers were the dominant precipitation source during the PETM (Shields et al., 2021). Overall, the climatic studies in the region indicate seasonality and an intensification of the hydrological cycle, consistent with global climatic models showing increased frequency and intensity of precipitation events in the Pyrenees (Rush et al., 2021).

While several assessments and models of the climatic evolution during the PETM have been achieved, how the MAP and rainfall distribution changed during this extreme warming event remains a significant issue. In the South-Pyrenean basin, questions concerning the local climatic disturbance, the temperature increase in the air and soil, and the intermittent nature of the precipitation maxima are still debated for the continental climatic regime in the South Pyrenees (Basilici et al., 2022; Chen et al., 2018; Rush et al., 2021; Schmitz & Pujalte, 2007). In this study, we bring insights into the response of the hydrological cycle to the extreme warming event based on clay mineralogy and clay $\delta^{18}O$ and δD composition in the Pre-, Syn- and Post-PETM paleosols of the Esplugafreda section (Figure 1) located in the Tremp basin. These new data will allow us to (a) constrain the local climatic perturbation in terms of temperature and precipitation, (b) calculate local temperature increase, and (c) define changes in weathering regime.

1.2. Isotopic Composition of Pedogenic Clays as a Paleoclimatic Proxy

Amongst clay minerals, pedogenic smectite is characteristic of poorly drained soils, indicative of a seasonally contrasted climate, and often associated with calcite nodules and hematite (Sheldon & Tabor, 2009; Tabor & Myers, 2015). Basilici et al. (2022) identified paleosol morphotypes as belonging to the Vertisols order based on mineralogical and morphological characteristics in the Esplugafreda section soils (e.g., Soil Survey Staff, 1999, 2022). The Vertisols along the Esplugafreda section consist of two phenotypes: (a) Pont d'Orrit, reddish horizons with calcareous nodules indicative of semi-arid conditions, and (b) Areny, yellowish horizons, rich in goethite and redoximorphic features, suggesting more humid (aquic) conditions (Basilici et al., 2022). Although paleosol morphology and clay mineralogy reflect pedogenetic processes and paleoenvironment conditions (e.g., Kraus, 1999; Tabor et al., 2008; Tabor & Myers, 2015), sediment supply, depositional setting, and length of pedogenesis could also affect their morphotype and maturity (McCarthy et al., 1998).

The oxygen and hydrogen isotopic composition of clay minerals formed in paleosols can be used to assess changes in temperature and precipitation conditions at the time of formation of the clays (limited in resolution by the rate of clay formation) (Bauer et al., 2016; Delgado & Reyes, 1996; Grujic et al., 2018; Rosenau & Tabor, 2013; Sheldon & Tabor, 2009). Paleosols form in direct equilibrium with contemporary climate conditions (e.g., Sheldon & Tabor, 2009). During clay formation, the parent rock constituting minerals, formed at high pressure and temperature conditions, undergoes a hydration process at surface conditions due to their interaction with the aqueous fluids out of the primary stability field of the mineral (Meunier, 2005). As equilibrium is reached, the amount of fluid increases, and the more soluble elements are removed from the primary minerals. The residue of more immobile elements constitutes secondary clay minerals. Different factors control the fractionation in the $\delta^{18}O$ and δD isotope fingerprints of the clays, some of them in opposing trends. The mineral-specific fractionation factors include (a) the isotopic composition of the meteoric water, (b) the temperature of the environment (air and soil) during clay formation, and (c) whether the clays reached isotopic equilibrium with the environment (Savin & Epstein, 1970; Sheppard & Gilg, 1996; Velde & Meunier, 2008). Pedogenic clay minerals retain their δD and $\delta^{18}O$ unless exposed to extreme diagenetic conditions (Sheppard & Gilg, 1996). Therefore, studying the isotopic composition of the smectite-rich clays has excellent potential as a paleoclimate proxy because they likely form in equilibrium with the Mean Annual Air Temperature (MAAT) (Bauer et al., 2016; Sheldon & Tabor, 2009).

2. Geological Context

The Pyrenees are associated with a history of strike-slip and convergence between the Iberian and the European continental plates, which took place from the Late Cretaceous to the Miocene (Angrand et al., 2020; Chevrot et al., 2018; Muñoz, 1992; Rosenbaum et al., 2002; Roure et al., 1989). However, the Paleocene corresponds to a relatively quiescent period (Rosenbaum et al., 2002). During the Paleocene, an extensive mixed clastic-carbonate
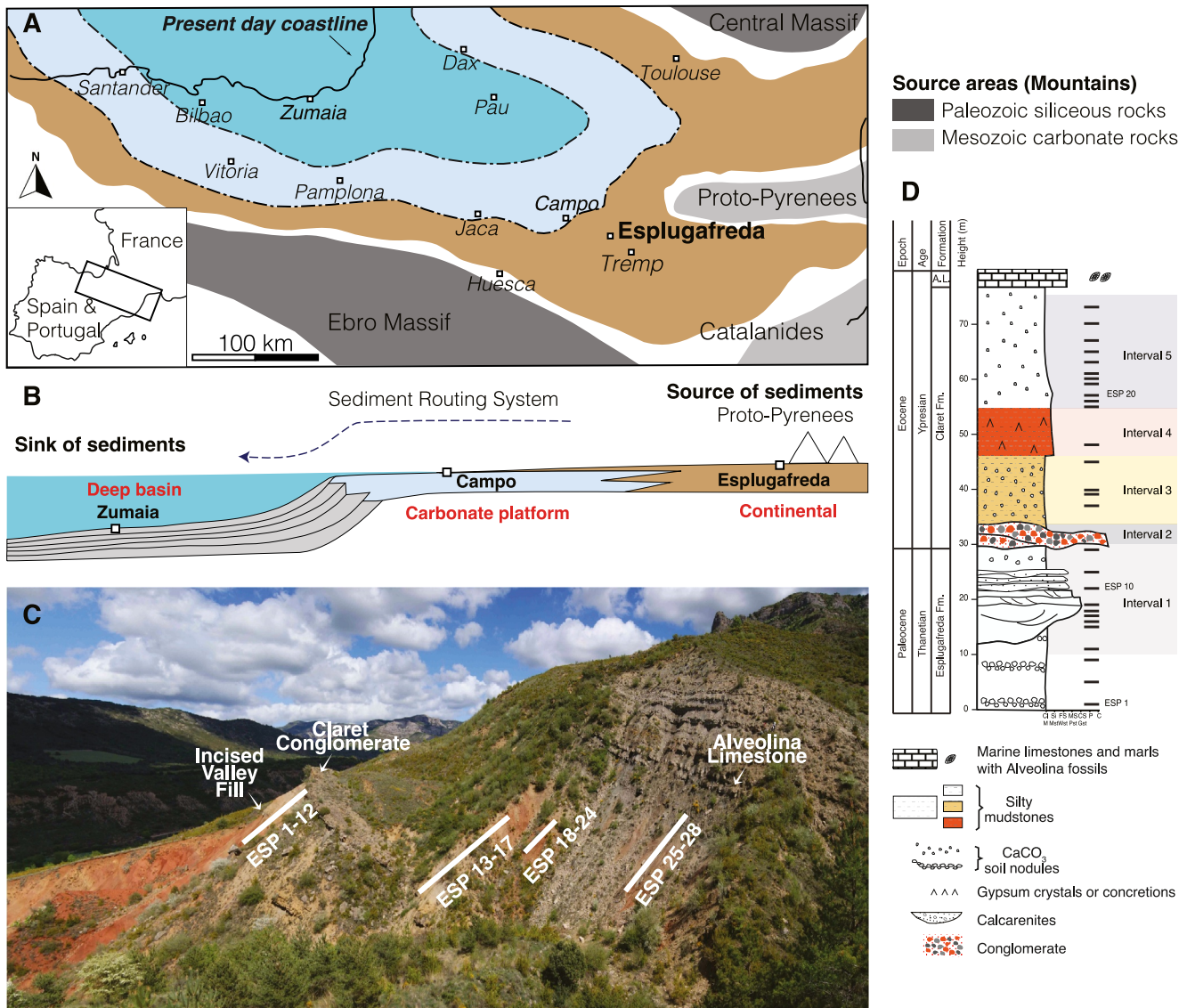
Figure 1. (a) Location of the study section (map of Spain) and paleogeography during the late Paleocene and early Eocene. Redrawn and modified from Pujalte et al. (2016). (b) Sediment routing system, modified from Tremblin et al. (2022). (c) Sampling divided into four transects. (d) Stratigraphy, modified from Khozyem (2013) and Pujalte et al. (2009) and sample distribution.

system, opening toward the west to the Atlantic Ocean, developed in front of the growing orogen. Shallow-marine limestones from a range of depositional environments (e.g., tidal flats, lagoons, shoals, reef buildups) and a minor share of siliciclastic and evaporitic rock (Baceta et al., 2011) emplaced coevally with a prominent continental system of transverse alluvial fans and axial streams corresponding to the Tremp Formation (Fm) and co-eval strata (Figure 1) (e.g., Dreyer, 1993; Schmitz & Pujalte, 2003, 2007).

This study focuses on the Esplugafreda and Claret formations from the Tremp-Graus basin, more precisely on the well-preserved continental deposits ranging from Thanetian to Ypresian age (Baceta et al., 2005; Colombera et al., 2017). The Esplugafreda Fm consists of a 165 m thick sequence of red mudstones, intercalated with sandy to conglomeratic channels and abundant carbonate nodules (Baceta et al., 2005, 2011; Schmitz & Pujalte, 2007). Pujalte et al. (2014) define the basal boundary of the Claret Fm as an erosional surface resulting from a sea-level drop and subsequent incision of a network of valleys.

The Esplugafreda section (Figure 1, coordinates: 42°14′50″N; 0°45′13″E) has been extensively studied and corresponds to the continental-most section of the well-preserved South Pyrenean Foreland Basin (e.g., Baceta

et al., 2005; Basilici et al., 2022; Khozyem, 2013; Pujalte et al., 2003; Schmitz & Pujalte, 2007; Tremblin et al., 2022). Several well-developed paleosols with preserved B horizons (see e.g., Kraus, 1999; Tabor & Myers, 2015 for paleosols horizonation in the geological record) are present throughout the sequence (Basilici et al., 2022). These paleosols are often rich in micritic (mm to cm long) and microcrystalline carbonate nodules (<3 mm in diameter) (Khozyem, 2013). Five distinct stratigraphic intervals have been recognized in this section (Figure 1d) (Baceta et al., 2011; Basilici et al., 2022; Colombera et al., 2017; Pujalte et al., 2009). Interval I consists of the Incised Valley Fill (IVF) in the upper part of the Esplugafreda Fm, capped by the Claret Fm. The IVF consists of an upward fining sequence of conglomerates and cross-laminated sandstones. Interval 1 can be subdivided into the Pre-PETM record and the Pre-Onset Excursion (POE), the first negative CIE in the record, during the late Paleocene (Khozyem, 2013; Tremblin et al., 2022). Interval 2 represents the Claret Conglomerate, a 3–5-m-thick clast-supported calcareous conglomerate. Interval 3 consists of 10–20-m-thick yellowish silty mudstone with purple mottling and dispersed carbonate nodules, with interbedded channelized sandstones. Interval 3 corresponds to the body of the PETM (Syn-PETM) (e.g., Baceta et al., 2011; Pujalte et al., 2009). Interval 4 consists of 10 m-thick red silty mudstones with a variable amount of gypsum. Interval 5 is a 20 m-thick light red mudstone with scarce carbonate nodules (Baceta et al., 2011). Intervals 4 and 5 constitute the recovery phase of the PETM in this section (Post-PETM). The Alveolina Limestone marks a transgressive event at the top of the Claret Formation (Baceta et al., 2011 and references therein).

3. Materials and Methods

3.1. Materials

The sample material (aliquots of 1–3 kg) consisting of clays-rich paleosols ($n = 28$) was collected from both the Esplugafreda and Claret formations (Figure 1), specifically in intervals 1, 3, 4, and 5. Interval 2 was not sampled due to the conglomeratic nature of the interval.

3.2. Methods

3.2.1. Size Fraction Separation

Decarbonization and size fraction separation were performed in the clay laboratory at the Institute of Earth Sciences at the University of Lausanne (ISTE, UNIL), following standard protocols (e.g., Adatte et al., 1996; Bauer et al., 2016). Approximately 5 g of sample were leached with 10% HCl for 30 min with a bubble bath, including a 3-min-long ultrasonic bath to disintegrate aggregations of sediments and dissolve calcite. The acid was then removed with distilled water until a neutral pH was measured and once the supernatant was cloudy. An aliquot of the decarbonated bulk rock was saved for later analyses. Subsequently, the <0.5 μm fraction was separated following Stokes law and enhanced with a centrifuge. This size fraction was removed three times, and the <2 μm fraction (depleted in the finer fraction) was separated from the bulk rock. Although the second fraction (0.5–2 μm) was depleted in <0.5 μm, we refer to it as <2 μm fraction, given that many more repetitions of the centrifugation would have been required to obtain a pure 0.5–2 μm fraction completely free of <0.5 μm clays. Size fraction separation for the bulk clay mineral assemblage (the entire <2 μm) was performed at Bio-géosciences, University of Burgundy, in an aliquot of the decarbonated samples from Lausanne. Based on Stokes's law, the clay-sized fraction was separated, calculating the time for the <2 μm particles to settle given a known height.

3.2.2. Clay Mineralogy

The clay minerals were identified on air-dried and ethylene glycol-solvated samples at ISTE (UNIL) following the protocol described in Adatte et al. (1996). An aliquot of the separated size fractions was pipetted on glass slides and dried at room temperature. The air-dried samples were further analyzed with a Thermo Scientific ARL X'TRA powder diffractometer equipped with a Cu anode, operated at 45 kV and 40 mA. The step size was 0.02°, with a 0.5–1.2°/min scan rate. Samples were glycolated to identify smectite (Moore & Reynolds, 1992). The diffractograms were then analyzed using the XRDWin software, where the background was removed, and a deconvolution was performed for overlapping peaks (e.g., K002 and Ch004). A Bruker Endeavor D4 diffractometer equipped with a Lynexeye detector, CuKa radiations, and Ni filter at 40 kV voltage and 25 mA intensity was used for characterizing the bulk clays (<2 μm) and the bulk rock at Biogéosciences, University of Burgundy. Clays were pipetted onto a glass plate, glycolate, and heated at 550°C. Bulk rocks were side-loaded onto metallic

holders for disoriented analyses. Semi-quantitative analyses were performed using the software MacDiff, using the position of mean diffraction peaks and the area of their main diffraction peak.

3.2.3. Stable Isotope Geochemistry

The 28 samples separated into two clay-size fractions were analyzed for oxygen and hydrogen isotopes at the Stable Isotope Laboratory at the Institute of Earth Surface Dynamics (IDYST, UNIL) (Bauer & Vennemann, 2014; Bauer et al., 2016; Lacroix & Vennemann, 2015; Sharp, 1990). To ensure the stable isotope measurements were performed on the structural water of the clay minerals, adsorbed water was removed from the samples by heating to 250°C for 3 hr while pumping to vacuum (Bauer et al., 2016). The oxygen isotope composition of the clay samples was measured with a CO_2 laser-based extraction line and F_2 as a reacting gas coupled to a Finnigan MAT 253 mass spectrometer. For details on the procedure at the University of Lausanne, see Lacroix and Vennemann (2015). Sample weights used vary between 1.0 and 2.5 mg.

Hydrogen mass spectrometry followed the method described by Bauer and Vennemann (2014). The δD and δ^{18}O were measured in a Thermo Finnigan MAT 253 isotope ratio mass spectrometer in dual inlet mode and are reported relative to Vienna Standard Mean Ocean Water (VSMOW) in delta notation.

The oxygen isotopes were corrected to the daily session value of the in-house quartz standard (LS-1) which was calibrated against the NBS-28 Quartz Standard with a value of 9.64‰ (Lacroix & Vennemann, 2015). The deviation to the accepted value of 18.1‰ is routinely better than 0.3‰; the standard deviation is routinely better than 0.2‰ (1σ) based on replicate analyses of the LS-1 standard. Duplicates of clay samples are better than 0.2‰. In-house standards used for hydrogen isotope mass spectrometry were Kaolinite 17, with a standard value of -120 ± 3.6‰ ($n = 31$), and Biotite G18526, with a standard value of -89.8 ± 2.4‰ ($n = 11$), with a clay sample duplicate reproducibility of ± 2‰.

3.2.4. Oxygen and Hydrogen Isotope Fractionation in Clay Minerals

Crystallization temperatures of the clay mineral assemblage were calculated (Craig, 1961; Dansgaard, 1964; Delgado & Reyes, 1996; Sheppard & Gilg, 1996; Yeh, 1979). The equations used assume a clay assemblage of 100% smectite. Therefore, after an initial analysis of all clay compositions, only the 15 samples containing a minimum of 80 wt% smectite (in the bulk clay assemblage) were considered. Two different approaches were implemented: (a) calculation of isotherms for smectite (Equations 1–5) and kaolinite (Sheppard & Gilg, 1996; Yeh, 1979), and (b) calculation of smectite crystallization temperature (Equation 6, Delgado & Reyes, 1996) using $\delta^{18}O_{smectite}$ and $\delta D_{smectite}$.

The δ^{18}O and δD of the smectite-rich samples allow calculation of the isotopic composition of water in equilibrium with the clay minerals at the time of formation. In the hydrological cycle, the δ^{18}O and δD of meteoric waters are linked, and the isotopic composition of the precipitations and of groundwaters are distributed along a line called the meteoric water line (Craig, 1961):

$$\delta D_{water} = 8\delta^{18}O_{water} + 10 \tag{1}$$

When applying Craig's equation (Equation 1), we assume that no evaporation takes place, and in doing so, we calculate a maximum temperature. Although carbonate nodules in the paleosols testify to the evaporation in the locality, their presence throughout the Pre- to Syn-PETM suggests that these assumptions would not affect the relative temperature changes temporally, though the absolute temperature will be overestimated. Developing the Sheppard and Gilg (1996) equation, where T_{soil} is the temperature (K) of the soil where clay mineralization occurs, the $\delta^{18}O_{water}$ can be derived as:

$$\delta^{18}O_{water} = -\frac{2.55 \times 10^6}{T_{soil}^2} + 4.05 + \delta^{18}O_{smectite} \tag{2}$$

Using Yeh (1979):

$$\delta D_{smectite} = -19.6 \times \frac{10^3}{T_{soil}} + 25 + \delta D_{water} \tag{3}$$

Replacing Equation 1 in Equation 3:

$$\delta D_{smectite} = -19.6 \times \frac{10^3}{T_{soil}} + 35 + 8\delta^{18}O_{water} \tag{4}$$

We then replace the $\delta^{18}O_{water}$ from Equation 2 in Equation 4 with temperature in Kelvin.

$$\delta D_{smectite} = -2.04 \times \frac{10^7}{T_{soil}^2} - 19.6 \times \frac{10^3}{T_{soil}} + 67.4 + 8\delta^{18}O_{smectite} \tag{5}$$

Equation 5 can be solved iteratively to calculate the soil crystallization temperature. Alternatively, the approach by Delgado and Reyes (1996) presents a single mineral geothermometer to estimate the smectite crystallization temperature based on the combined oxygen and hydrogen isotope composition of this clay mineral. Equation 6 allows the calculation of the clay crystallization temperature (K) using $\delta^{18}O_{smectite}$ and $\delta D_{smectite}$.

$$3.54 \times 10^6 T_{soil}^{-2} = \delta^{18}O_{smectite} - 0.125\delta D_{smectite} + 8.95 \tag{6}$$

4. Results

4.1. Clay Assemblages and Bulk Rock Mineralogy

The bulk clay mineralogy is characterized by a high and relatively constant smectite and mixed-layer illite/smectite of more than 80 wt% through intervals 1 to 3 (Figure 2). Smectite fluctuates above 80% during Interval 1 and remains dominant during Interval 3 (the body of the PETM, Figure 2). Intervals 4 and 5 are characterized by decreased smectite content and a coeval increase of kaolinite, illite, and chlorite. Results on the <0.5 μm and <2 μm are reported in Supporting Information S1.

The bulk rock mineralogy (see Supporting Information S1) is dominated by more than 50 wt% calcite, which consistently increases from the base of the section until Interval 5, reaching more than 70 wt%. Clays account for about 35 wt% at the base of the section, decreasing to around 12 wt% toward the top. Quartz is relatively constant at approximately 10 wt%, while feldspar remains below 5 wt%. The plagioclase versus K-feldspar shows a positive peak around the yellowish soils (35–48 m). Goethite increased from 3 to 10 wt% in Interval 4.

4.2. Stable Isotopes

The $\delta^{18}O$ varies from 18.1 to 20.9‰, while the δD in the section ranges from −83 to −64‰ (Figure 3). Oxygen isotopes between the two size fractions show an almost identical evolution (within analytical error). Hydrogen isotopes, on the contrary, show a distinct lag between the two size fractions before the POE and after Interval 4. In the <0.5 μm fraction, Interval 1 (excluding the POE record) had an average $\delta^{18}O$ composition of 19.6‰ with a standard deviation (σ) of 0.3 and a δD of −75.2‰, with σ of 5.2. The segment of Interval 1 corresponding to the POE had an average $\delta^{18}O$ of 20.3‰ with σ of 0.5, and a δD of −77.7‰ with σ of 3.7. Interval 3 had an $\delta^{18}O$ of 19.7‰ with σ of 0.5, and δD of −76.8 with σ 4.2. At last, intervals 4 and 5 had an $\delta^{18}O$ of 18.5‰ with a σ of 0.3, and δD of −71.0‰ with σ of 3.3. Intervals 1 POE and three show two distinct positive $\delta^{18}O$ excursions.

The δD versus $\delta^{18}O$ shows distinct populations for each interval, with lower δD values for the <2 μm size fraction (Figure 4). The Pre-PETM $\delta^{18}O$ has an average of 19.7‰ VSMOW in both size fractions, with δD being about −75‰ VSMOW and −79‰ VSMOW for the <0.5 and <2 μm, respectively. The POE and the Syn-PETM record show more positive values in the $\delta^{18}O$. The δD record is more negative for the <2 μm size fractions during the Syn- than Pre-PETM, with larger variations during the Pre-PETM in the <0.5 μm fraction. The behavior between the two clay-size fractions has an opposing trend during the POE. During the Post-PETM, Interval 5, both size fractions show the lowest $\delta^{18}O$ values, with the δD record for the finer size fraction having the less negative values.
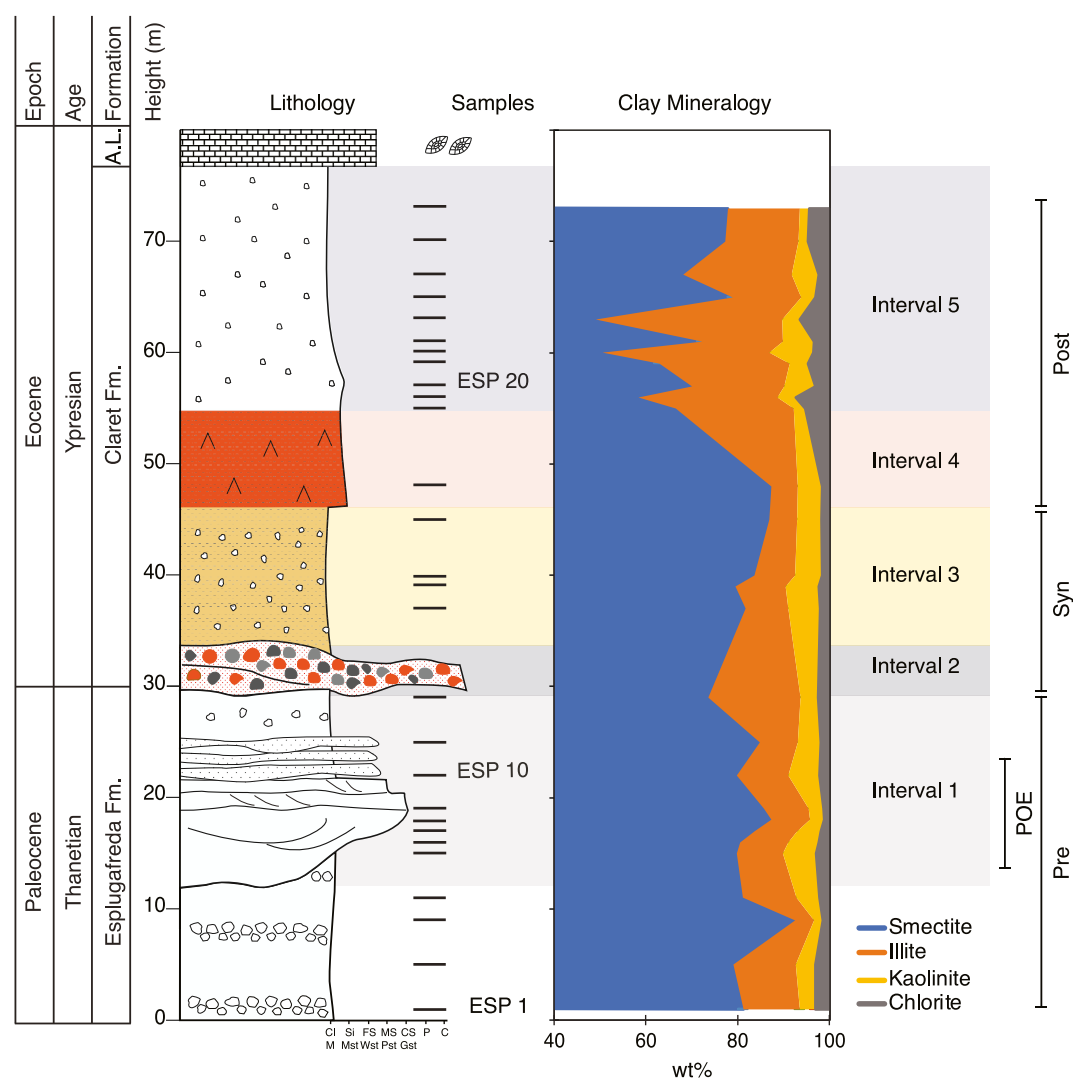
Figure 2. Esplugafreda section cumulative clay mineralogy. The clay mineralogy assemblage is dominated by smectite throughout the section, with a constant amount during the Pre- and Syn-PETM (intervals 1 and 3) and a decrease in smectite during the Post-PETM (intervals 4 and 5). Illite, kaolinite, and chlorite are present in minor amounts, peaking during intervals 4 and 5.

5. Discussion

5.1. Clay Assemblages and Paleoclimate Conditions

Pedogenic smectite, as seen in the Esplugafreda section, forms in poorly drained soils with strong seasonal precipitations (Sheldon & Tabor, 2009). Although kaolinite is abundant in paleosol profiles in paleotropical sites (Meunier, 2005; Velde & Meunier, 2008), it can be a minor constituent in soils dominated by 2:1 clay minerals (Sheldon & Tabor, 2009). The clay assemblage in paleosols is a mixture of pedogenic, detrital, and diagenetic clays (Grujic et al., 2018). Furthermore, the clays form in or close to isotopic equilibrium with meteoric waters and record surface environmental conditions (Bauer et al., 2016; Rosenau & Tabor, 2013; Sheppard & Gilg, 1996). The general smectite-rich assemblage here suggests a predominantly pedogenetic origin (Chamley, 1989), further supported by Scanning Electron Microscopy (SEM) images showing preserved authigenic mineral structures of the smectite (Supporting Information S1).

A first estimate of annual precipitation conditions can be obtained from the morphotype of the palaeosols (Basilici et al., 2022). Interval 1, rich in smectite with abundant carbonate nodules, can be interpreted as a Calcic Vertisol, thus suggesting subhumid to semiarid environments with seasonal precipitation and drainage (Tabor &
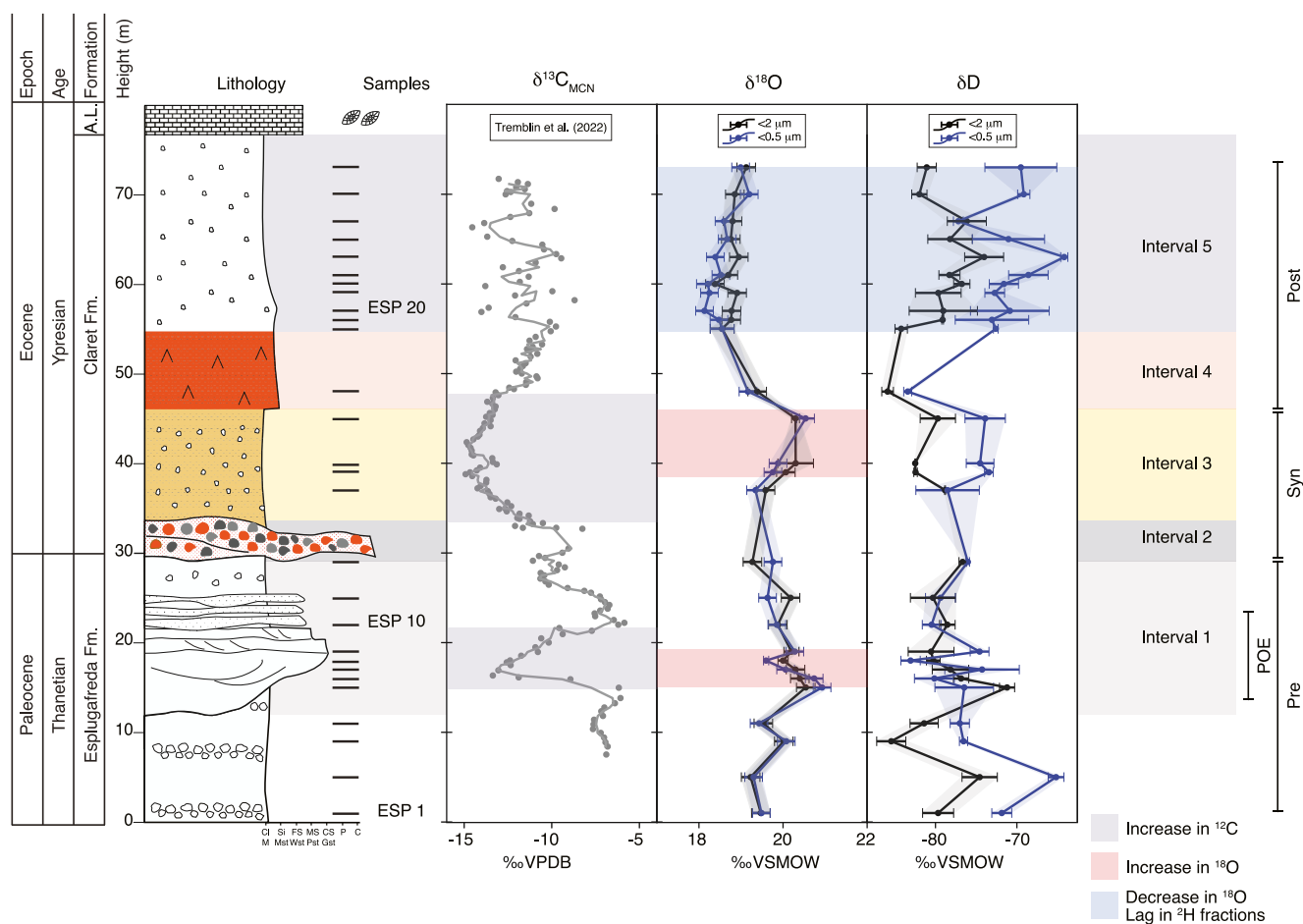
ET AL.

Figure 3. Stable isotope climatic proxies. The carbon isotopes from Tremblin et al. (2022) mark the different sections of the PETM. The δD and δ^{18}O were measured in two size fractions, <0.5 and <2 μm. The confidence interval for δ^{18}O constitutes the analytical uncertainty (0.2‰) and that of δD constitutes the sample replicate reproducibility.

Myers, 2015; Tabor et al., 2008). The formation of carbonate nodules, an evaporative feature in Calcic Vertisols, suggests a relatively dry climate with seasonal or annual aridity (Sheldon & Tabor, 2009; Tabor et al., 2008). Although it has been suggested that Vertisols are unreliable indicators of climate (Thiry, 2000), pedogenic carbonate nodules, in combination with soil abundance and mineralogy, suggest that they are a reliable seasonal indicator (Chamley, 1989; Khozyem, 2013; Schmitz & Pujalte, 2007). Based on channel dimensions and sediment grain size, Interval 2 has been interpreted as a massive discharge event (e.g., Chen et al., 2018; Schmitz & Pujalte, 2007). Interval 3 displays a characteristic yellowish color with mottling, a feature indicating reducing conditions with periodic to complete water soil saturation and a sustained enrichment in smectite (Pujalte et al., 2014; Schmitz & Pujalte, 2003, 2007). The reducing condition suggests that Interval 3 has the highest hydrolyzing potential, in agreement with Basilici et al. (2022).

Intervals 4 and 5 are interpreted as Gypsic Vertisols, suggesting a more aridic climate (Tabor & Myers, 2015). However, gypsum could reflect post-depositional precipitation (Basilici et al., 2022). In a post-depositional precipitation scenario, one would expect gypsum to be present throughout the entire Esplugafreda section and not only in the interval pointing to more aridic conditions. Therefore, the primary precipitation hypothesis is preferred. The thermodynamic conditions at which gypsum and anhydrite can coexist in equilibrium have been recently estimated to be 42 ± 1°C (Voigt & Freyer, 2023). The absence of anhydrite and gypsum preservation, suggests that the clays were not subject to diagenesis and, therefore, preserved the climatic signal. In modern soils, gypsum nodules are unlikely to be preserved if rainfall exceeds 300 mm/yr, thus indicative of arid conditions (Tabor & Myers, 2015; Watson, 1992). While soil morphotypes can inform about past climate variability,
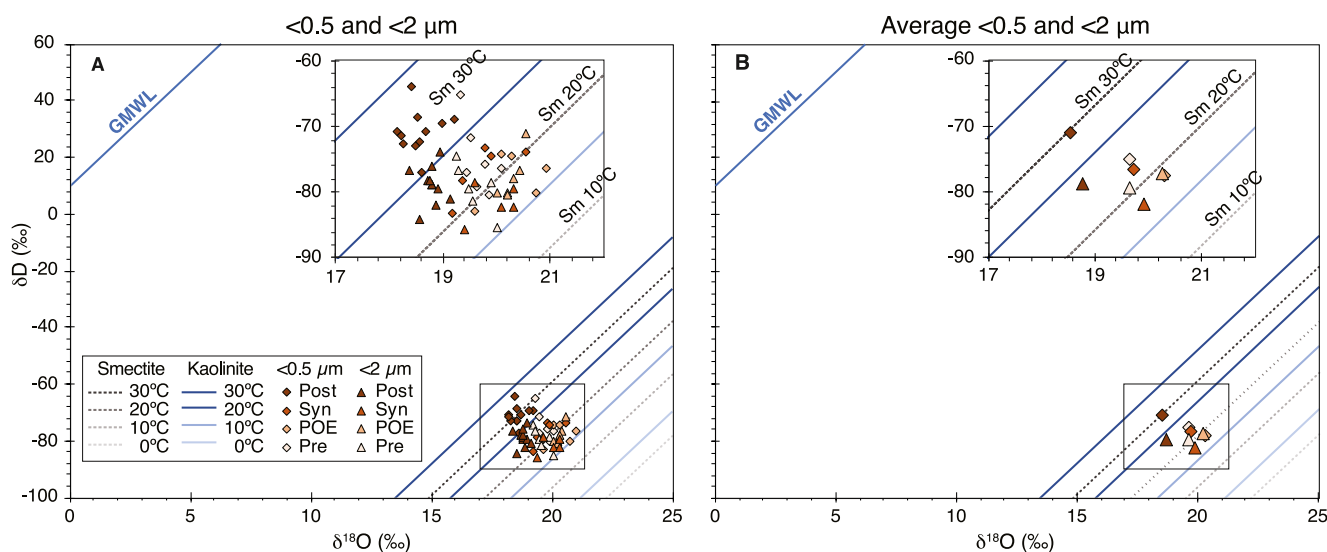
Figure 4. Cross plots of the δD versus δ^{18}O of clays, color, and symbol coded according to the different intervals described. (a) Presents all the data points in both size fractions, and (b) displays the average isotopic composition in each interval for each size fraction. Data points in the two size fractions are coded according to the period relative to the PETM. Global Meteoric Water Line (GMWL) and isotherms for kaolinite and smectite at 0, 10, 20, and 30°C from Sheppard and Gilg (1996) and Yeh (1979). The kaolinite isotherms have a lower δ^{18}O for the same crystallization temperatures. Hence, the cluster of the Post-PETM to the left of the Syn- and Pre-PETM clusters reflects a change in the mineralogy. (b) Average values in each size fraction for the four periods.

Vertisols can develop under various climatic regimes with strong seasonality (Basilici et al., 2022 and references therein).

5.2. Oxygen and Hydrogen Isotopic Composition of Paleo-Meteoric Water

The Esplugafreda section records two δ^{18}O positive excursions, one coinciding with the POE (Interval 1) and one during the PETM (Interval 3) (Figure 3). Both δ^{18}O positive excursions are associated with negligible variations in δD (Figure 3). The variations in δ^{18}O could be either explained by (a) an increase in air temperature, globally recorded during the POE and the PETM, (b) a decrease in soil temperature, or (c) a decrease in water saturation of the soils (either by a decrease in rainfall or an increase in evaporation) (Bauer et al., 2016). The δD isotopes could reflect two processes at surface conditions, an increase in rainfall or a mineralogical change (Merseburger, 2022; Sheppard & Gilg, 1996). The δD in kaolinite, smectite, and illite is relatively insensitive to temperature changes (0–350°C) (Merseburger, 2022). Hence, the stability in the δD during the POE and body of the PETM, as opposed to δ^{18}O positive excursions, suggest a temperature-controlled climatic change, that is, an increase in the air temperature in the catchment area and floodplain deposits where pedogenesis took place during the POE and the PETM.

Sample clusters on the smectite and kaolinite lines (Figure 4) give a first clay crystallization temperature. The Pre-PETM samples fall on the smectite crystallization line at 20°C (Figure 4a). Interval 1, POE samples, and Interval 3, Syn-PETM samples, suggest roughly the same temperature of 20°C. However, intervals 4 and 5 (Post-PETM) samples fall closer to the 30°C smectite line. Intervals 4 and 5 also correspond to a decrease in smectite and an increase in illite and kaolinite relative proportions in the mineral assemblage (Figure 3). As kaolinite records lower δ^{18}O values and/or higher δD than smectites when formed in the same environmental conditions, a soil temperature overestimation has been found experimentally in smectite-rich soils containing illite and kaolinite (Myers et al., 2012). In addition, the concomitant increase in illite and kaolinite proportions, two clay minerals that form in different environmental conditions, suggest that some of the clays from intervals 4 to 5 are reworked from ancient sediments, therefore recording different water isotopic composition and temperature than the pedogenic smectites. Therefore, the decrease in δ^{18}O, as well as the lag between the two clay size fractions in δD (Figure 3), could reflect a change in the clay mineral assemblage with an increase in illite and kaolinite and a decrease in smectite rather than a change in temperature or precipitation amount. This mineral assemblage change is interpreted as an increase in detrital input exhuming older clays, which were formed under a different climatic regime.
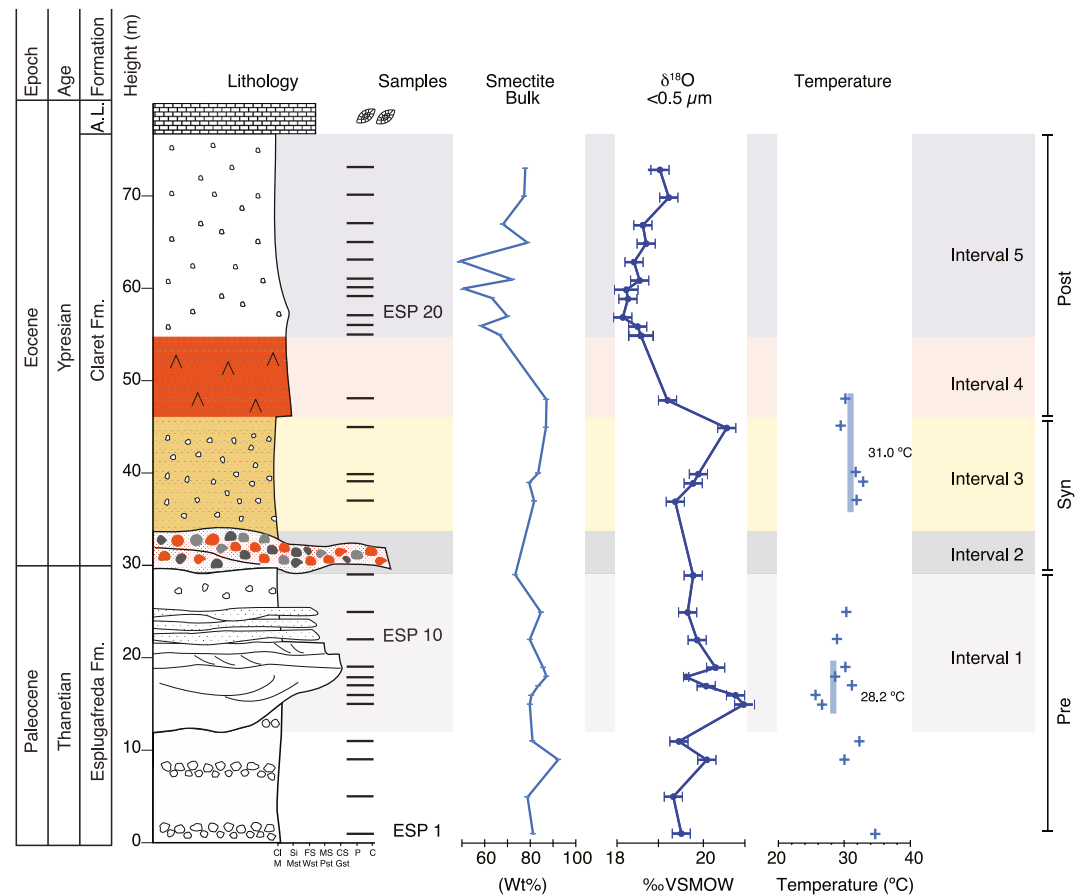
Figure 5. Single-mineral geothermometer from Delgado and Reyes (1996) calculated with the $\delta^{18}O$ and δD measured in clays (<0.5 μm fraction) for bulk clays containing more than 80% smectite. From left to right, lithology, smectite content through the section, $\delta^{18}O$ smectite of the <0.5 μm clay fraction, and crystallization temperature calculated with Equation 6. For the POE, we calculated a relative error of 1.0°C, a standard deviation of 2.1°C, and an average Monte Carlo error propagation of 3.0°C. For the Syn-PETM, we calculate a relative error of 0.8°C, a standard deviation of 1.3°C, and an average Monte Carlo error propagation of 2.5°C.

Clay crystallization temperature can be used as a proxy for air temperature, assuming that $T_{air} < T_{soil}$, especially for dry and warm environments (García-García et al., 2023; Molnar, 2022). For the clay crystallization temperature calculated after Delgado and Reyes (1996), we assume that soil temperature reflects the MAAT at equilibrium with the meteoric water with which the clays formed (e.g., Bauer et al., 2016; Grujic et al., 2018; Sheppard & Gilg, 1996). Given the clay mineral composition variability and the accumulated error propagation, we consider only soil crystallization temperatures for the POE and the Syn-PETM, which had the highest smectite proportions. Hence, the fractionation equations used applied the best. The variability of the detrital clay minerals in the rest of the section renders the accumulated error (when accounting for δD, $\delta^{18}O$, and fractionation factors for varying proportions of clay minerals) too large to be considered. Using the Delgado and Reyes geothermometer for smectite, we calculate a soil crystallization temperature of 28.2°C during the POE, with a standard deviation of 2.1°C (1σ) and an average Monte Carlo error propagation of 3.0°C (see Supporting Information S1 for Python code). For the Syn-PETM, we calculate a soil crystallization temperature of 31.0°C, with a 1.3°C (1σ) and an average Monte Carlo error propagation of 2.5°C. We calculate a relative error (analytical error for a given isotope and the isotope value in relation to the crystallization temperature calculated) of 1.0°C for the POE and 0.8°C for the Syn-PETM. We calculate the air temperature using the calculated POE clay crystallization temperature of 28.2 ± 1.0°C and a Syn-PETM of 31.0 ± 0.8°C (Figure 5). Applying the $\Delta T = T_{soil}-T_{air}$ for dry and arid environments of 4°C (Gallagher et al., 2019; Molnar, 2022), the POE MAAT obtained is 24.2 ± 1.0°C and Syn-PETM of 27.0 ± 0.8°C. These results are consistent with the modeled MAAT in this region (Rush et al., 2021). The calculated temperature increase is a lower threshold because the smectite abundance ranges

between 80% and 93% in intervals 1 and 3. Hence, the uncertainty of the temperatures presented here is directly linked to the changes in the clay mineral assemblage. Uncertainty increases with decreasing proportions of smectite and increasing proportions of illite, kaolinite, and chlorite (reflecting different age populations and crystallization temperatures). Comparing the crystallization temperature estimates with Equations 5 and 6 results in different temperatures, and it can be attributed to the natural variation in the composition of the smectites used for the fractionation factor calculations and the difference in the slope of the equations used. However, considering the relative temperature changes instead of the absolute temperature estimations serves as a first approach to understanding the magnitude of the local air temperature variation.

The Areny Vertisols characteristic of the Syn-PETM (Interval 3) indicates more humid conditions (Basilici et al., 2022), thus affecting the local climate and the isotopic record in the clays. Under warm and seasonally wet conditions, soil temperatures can be cooled by releasing latent heat by evaporation of the moist soils, increasing the soil's water content and precipitation rates (García-García et al., 2023). The water saturation buffers temperature fluctuations in the soil. The Syn-PETM Interval 3 would be, therefore, characterized by warm temperatures with intense rainfall events, as indicated by the channel width and grain size evolution (Chen et al., 2018; Pujalte et al., 2015; Schmitz & Pujalte, 2007). Overall, the precipitation regime during Interval 3, the body of the PETM, led to more extreme precipitation events but not an increase in the MAP, given the stable $\delta^{18}O$ composition observed during this interval.

Conversely, during PETM recovery, intervals 4 and 5 in the Pont d'Orrit pedotype (Basilici et al., 2022), local trends show a pattern of aridification supported by the abundant gypsum in the soils. The decrease in $\delta^{18}O$ values in both clay-sized fractions could also reflect aridification, but quantification is difficult due to the mixed authigenic and detrital nature of the clays in this interval. Net radiation could have further warmed the soil temperature as a result of the increased air temperature during the body of the PETM, resulting in desiccated soils by the recovery phase (García-García et al., 2023). This soil desiccation would further limit moisture availability. The aridification driver could have been, therefore, a lack of a local moisture source despite the increased water-holding capacity (Coumou & Rahmstorf, 2012; Held & Soden, 2006). The gypsum present in this interval is either of authigenic origin, indicative of more aridic conditions (Khozyem, 2013; Schmitz & Pujalte, 2007), or secondary origin resulting from the oxidation of pyrite (Basilici et al., 2022). The absence of gypsum in the lower horizons supports the first hypothesis.

Our data suggest that the climatic disturbance was primarily controlled by temperature fluctuation during the POE and the Syn-PETM. The stratigraphic record indicates a hydrological disturbance characterized by episodic rainfalls and a subsequent increase in the sediment fluxes to the deep ocean (Chen et al., 2018; Prieur et al., 2024), which Schmitz and Pujalte (2007) describe as high-energy floods linked with high-flux precipitation of short duration. However, these perturbations do not reflect a mean annual increase in precipitation but rather extreme short-lived events, consistent with an increase in the seasonality and intensity of precipitation events (Rush et al., 2021; Shields et al., 2021). One implication for the denudation regime includes an increase in the rainwater's carbonating capacity, which controls the weathering front (Maher, 2010). Given the increase in erosion rates, the kinetics of the mineral reactions would be the limiting factor in this climatic regime (e.g., Gabet & Mudd, 2009; Riebe et al., 2004; West et al., 2005). Silicate weathering has increased in other sections worldwide during the PETM, for example, Svalbard, Fur, and the Big Horn Basin (Pogge von Strandmann et al., 2021; Ramos et al., 2022). Further research is crucial to understand how silicate weathering has changed under different climatic regimes, such as the semi-arid conditions in the Southern Pyrenees. Understanding the weathering regime is essential for recognizing the role of denudation in recovering the climate to pre-warming conditions.

6. Conclusions

The combination of hydrogen (δD) and oxygen ($\delta^{18}O$) isotopes in clays and the different fractionation factors suggest that changes in MAAT, rather than changes in MAP, have characterized local climatic disturbances in the Southern Pyrenees. The positive $\delta^{18}O$ excursion and negligible δD change during the POE and Syn-PETM (Interval 3, body of the PETM), together with the high authigenic clay mineral production of smectite suggest a MAAT increase. We calculate a POE clay crystallization temperature of 28.2 ± 1.0°C and a MAAT of 24.2 ± 1.0°C. For the Syn-PETM, we estimate a clay crystallization temperature of 31.0 ± 0.8°C, with a MAAT of 27.0 ± 0.8°C. The variability in clay minerals composition limits these minimum temperature estimates.

The PETM in the Tremp-Graus basin was characterized by massive precipitation events, as recorded in the literature, with negligible variations in the MAP based on the minor variations in the δD during the Syn-PETM. Water availability, not atmospheric carrying capacity, would have been the limiting factor for a MAP increase. At Esplugafreda, air and soil temperature increase, desiccation of the soils, and reduced water availability in the soils played a positive feedback role in the climate aridification during the recovery phase of the PETM. The increase in extreme rainfall events suggests a denudation regime in which mineral kinetics rather than transport capacity governed the silicate weathering efficiency. The silicate weathering regime needs to be further analyzed with additional weathering proxies that quantify the amount of chemical alteration of paleosols in relation to the erosional capacity of the system.

Data Availability Statement

The data used in this study are available at Zenodo (Jaimes-Gutierrez et al., 2024). The Python code for running the Monte Carlo simulation for Equations 5 and 6 is available at Zenodo (Jaimes-Gutierrez & Wild, 2024).

References

Adatte, T., Stinnesbeck, W., & Keller, G. (1996). Lithostratigraphic and mineralogic correlations of near K/T boundary clastic sediments in northeastern Mexico: Implications for origin and nature of deposition. In G. Ryder, D. E. Fastovsky, & S. Gartner (Eds.), *The cretaceous-tertiary event and other catastrophes in Earth history*. Geological Society of America. https://doi.org/10.1130/0-8137-2307-8.211

Angrand, P., Mouthereau, F., Masini, E., & Asti, R. (2020). A reconstruction of Iberia accounting for Western Tethys–North Atlantic kinematics since the late-Permian–Triassic. *Solid Earth*, *11*, 1313–1332. https://doi.org/10.5194/se-11-1313-2020

Baceta, J. I., Pujalte, V., & Bernaola, G. (2005). Paleocene coralgal reefs of the western Pyrenean basin, northern Spain: New evidence supporting an earliest Paleogene recovery of reefal ecosystems. *Palaeogeography, Palaeoclimatology, Palaeoecology*, *224*(1–3), 117–143. https://doi.org/10.1016/j.palaeo.2005.03.033

Baceta, J. I., Pujalte, V., Wright, V. P., & Schmitz, B. (2011). Carbonate platform models, sea/level changes and extreme climatic events during the Paleocene/Eocene greenhouse interval: A basin-platform-coastal plain transect across the southern Pyrenean basin. In *28th IAS Meeting of Sedimentology*.

Basilici, G., Colombera, L., Soares, M. V. T., Arévalo, O. J., Mountney, N. P., Lorenzoni, P., et al. (2022). Variations from dry to aquic conditions in Vertisols (Esplugafreda Formation, Eastern Pyrenees, Spain): Implications for late Paleocene climate change. *Palaeogeography, Palaeoclimatology, Palaeoecology*, *595*, 110972. https://doi.org/10.1016/j.palaeo.2022.110972

Bauer, K. K., & Vennemann, T. W. (2014). Analytical methods for the measurement of hydrogen isotope composition and water content in clay minerals by TC/EA. *Chemical Geology*, *363*, 229–240. https://doi.org/10.1016/j.chemgeo.2013.10.039

Bauer, K. K., Vennemann, T. W., & Gilg, H. A. (2016). Stable isotope composition of bentonites from the Swiss and Bavarian Freshwater Molasse as a proxy for paleoprecipitation. *Palaeogeography, Palaeoclimatology, Palaeoecology*, *455*, 53–64. https://doi.org/10.1016/j.palaeo.2016.02.002

Bolle, M.-P., & Adatte, T. (2001). Palaeocene-early Eocene climatic evolution in the Tethyan realm: Clay mineral evidence. *Clay Minerals*, *36*(2), 249–261. https://doi.org/10.1180/000985501750177979

Bolle, M.-P., Pardo, A., Hinrichs, K.-U., Adatte, T., Von Salis, K., Burns, S., et al. (2000). The Paleocene-Eocene transition in the marginal northeastern Tethys (Kazakhstan and Uzbekistan). *International Journal of Earth Sciences*, *89*(2), 390–414. https://doi.org/10.1007/s005310000092

Bornemann, A., Norris, R. D., Lyman, J. A., D'haenens, S., Groeneveld, J., Röhl, U., et al. (2014). Persistent environmental change after the Paleocene–Eocene Thermal Maximum in the Eastern North Atlantic. *Earth and Planetary Science Letters*, *394*, 70–81. https://doi.org/10.1016/j.epsl.2014.03.017

Bowen, G. J., & Zachos, J. C. (2010). Rapid carbon sequestration at the termination of the Palaeocene–Eocene Thermal Maximum. *Nature Geoscience*, *3*(12), 866–869. https://doi.org/10.1038/ngeo1014

Bralower, T. J., Kump, L. R., Self-Trail, J. M., Robinson, M. M., Lyons, S., Babila, T., et al. (2018). Evidence for shelf acidification during the onset of the Paleocene-Eocene Thermal Maximum. *Paleoceanography and Paleoclimatology*, *33*(12), 1408–1426. https://doi.org/10.1029/2018PA003382

Burgener, L., Huntington, K. W., Hoke, G. D., Schauer, A., Ringham, M. C., Latorre, C., & Díaz, F. P. (2016). Variations in soil carbonate formation and seasonal bias over >4 km of relief in the western Andes (30°S) revealed by clumped isotope thermometry. *Earth and Planetary Science Letters*, *441*, 188–199. https://doi.org/10.1016/j.epsl.2016.02.033

Carmichael, M. J., Inglis, G. N., Badger, M. P. S., Naafs, B. D. A., Behrooz, L., Remmelzwaal, S., et al. (2017). Hydrological and associated biogeochemical consequences of rapid global warming during the Paleocene-Eocene Thermal Maximum. *Global and Planetary Change*, *157*, 114–138. https://doi.org/10.1016/j.gloplacha.2017.07.014

Carmichael, M. J., Pancost, R. D., & Lunt, D. J. (2018). Changes in the occurrence of extreme precipitation events at the Paleocene–Eocene thermal maximum. *Earth and Planetary Science Letters*, *501*, 24–36. https://doi.org/10.1016/j.epsl.2018.08.005

Chamley, H. (1989). *Clay sedimentology*. Springer Berlin Heidelberg. https://doi.org/10.1007/978-3-642-85916-8

Charles, A. J., Condon, D. J., Harding, I. C., Pälike, H., Marshall, J. E. A., Cui, Y., et al. (2011). Constraints on the numerical age of the Paleocene-Eocene boundary: Age of the P-E boundary. *Geochemistry, Geophysics, Geosystems*, *12*(6), Q0AA17. https://doi.org/10.1029/2010GC003426

Chen, C., Guerit, L., Foreman, B. Z., Hassenruck-Gudipati, H. J., Adatte, T., Honegger, L., et al. (2018). Estimating regional flood discharge during Palaeocene-Eocene global warming. *Scientific Reports*, *8*(1), 13391. https://doi.org/10.1038/s41598-018-31076-3

Chevrot, S., Sylvander, M., Diaz, J., Martin, R., Mouthereau, F., Manatschal, G., et al. (2018). The non-cylindrical crustal architecture of the Pyrenees. *Scientific Reports*, *8*(1), 9591. https://doi.org/10.1038/s41598-018-27889-x

Clyde, W. C., & Gingerich, P. D. (1998). Mammalian community response to the latest Paleocene thermal maximum: An isotaphonomic study in the northern Bighorn Basin, Wyoming. *Geology*, *26*(11), 1011. https://doi.org/10.1130/0091-7613(1998)026<1011:MCRTTL>2.3.CO;2

Colombera, L., Arévalo, O. J., & Mountney, N. P. (2017). Fluvial-system response to climate change: The Paleocene-Eocene Tremp Group, Pyrenees, Spain. *Global and Planetary Change*, *157*, 1–17. https://doi.org/10.1016/j.gloplacha.2017.08.011

Coumou, D., & Rahmstorf, S. (2012). A decade of weather extremes. *Nature Climate Change*, *2*(7), 491–496. https://doi.org/10.1038/nclimate1452

Craig, H. (1961). Isotopic variations in meteoric waters. *Science*, *133*(3465), 1702–1703. https://doi.org/10.1126/science.133.3465.1702

Cui, Y., Kump, L. R., Ridgwell, A. J., Charles, A. J., Junium, C. K., Diefendorf, A. F., et al. (2011). Slow release of fossil carbon during the Palaeocene–Eocene Thermal Maximum. *Nature Geoscience*, *4*(7), 481–485. https://doi.org/10.1038/ngeo1179

Dansgaard, W. (1964). Stable isotopes in precipitation. *Tellus*, *16*(4), 436–468. https://doi.org/10.1111/j.2153-3490.1964.tb00181.x

Delgado, A., & Reyes, E. (1996). Oxygen and hydrogen isotope compositions in clay minerals: A potential single-mineral geothermometer. *Geochimica et Cosmochimica Acta*, *60*(21), 4285–4289. https://doi.org/10.1016/S0016-7037(96)00260-8

Dickens, G. R., O'Neil, J. R., Rea, D. K., & Owen, R. M. (1995). Dissociation of oceanic methane hydrate as a cause of the carbon isotope excursion at the end of the Paleocene. *Paleoceanography*, *10*(6), 965–971. https://doi.org/10.1029/95PA02087

Donat, M. G., Lowry, A. L., Alexander, L. V., O'Gorman, P. A., & Maher, N. (2017). Addendum: More extreme precipitation in the world's dry and wet regions. *Nature Climate Change*, *7*(2), 154–158. https://doi.org/10.1038/nclimate3160

Dreyer, T. (1993). Quantified fluvial architecture in ephemeral stream deposits of the Esplugafreda Formation (Palaeocene), Tremp-Graus Basin, Northern Spain. In M. Marzo & C. Puigdefábregas (Eds.), *Alluvial sedimentation* (1st ed., pp. 337–362). Wiley. https://doi.org/10.1002/9781444303995.ch23

Dunkley Jones, T., Manners, H. R., Hoggett, M., Kirtland Turner, S., Westerhold, T., Leng, M. J., et al. (2018). Dynamics of sediment flux to a bathyal continental margin section through the Paleocene–Eocene Thermal Maximum. *Climate of the Past*, *14*(7), 1035–1049. https://doi.org/10.5194/cp-14-1035-2018

Dypvik, H., Riber, L., Burca, F., Rüther, D., Jargvoll, D., Nagy, J., & Jochmann, M. (2011). The Paleocene–Eocene thermal maximum (PETM) in Svalbard—Clay mineral and geochemical signals. *Palaeogeography, Palaeoclimatology, Palaeoecology*, *302*(3–4), 156–169. https://doi.org/10.1016/j.palaeo.2010.12.025

Edenhofer, O., Pichs-Madruga, R., Sokona, Y., Farahani, E., Kadner, S., Seyboth, K., et al. (2014). IPCC, 2014: Summary for policymakers. In *Climate Change 2014: Mitigation of Climate Change. Contribution of Working Group III to the Fifth Assessment Report of the Intergovernmental Panel on Climate Change*. Cambridge University Press.

Foreman, B. Z. (2014). Climate-driven generation of a fluvial sand body at the Paleocene-Eocene boundary in north-west Wyoming (USA). *Basin Research*, *26*(2), 225–241. https://doi.org/10.1111/bre.12027

Foreman, B. Z., Heller, P. L., & Clementz, M. T. (2012). Fluvial response to abrupt global warming at the Palaeocene/Eocene boundary. *Nature*, *491*(7422), 92–95. https://doi.org/10.1038/nature11513

Gabet, E. J., & Mudd, S. M. (2009). A theoretical model coupling chemical weathering rates with denudation rates. *Geology*, *37*(2), 151–154. https://doi.org/10.1130/G25270A.1

Gallagher, T. M., Hren, M., & Sheldon, N. D. (2019). The effect of soil temperature seasonality on climate reconstructions from paleosols. *American Journal of Science*, *319*(7), 549–581. https://doi.org/10.2475/07.2019.02

Gallagher, T. M., & Sheldon, N. D. (2016). Combining soil water balance and clumped isotopes to understand the nature and timing of pedogenic carbonate formation. *Chemical Geology*, *435*, 79–91. https://doi.org/10.1016/j.chemgeo.2016.04.023

García-García, A., Cuesta-Valero, F. J., Miralles, D. G., Mahecha, M. D., Quaas, J., Reichstein, M., et al. (2023). Soil heat extremes can outpace air temperature extremes. *Nature Climate Change*, *13*(11), 1237–1241. https://doi.org/10.1038/s41558-023-01812-3

Gariano, S. L., & Guzzetti, F. (2016). Landslides in a changing climate. *Earth-Science Reviews*, *162*, 227–252. https://doi.org/10.1016/j.earscirev.2016.08.011

Grujic, D., Govin, G., Barrier, L., Bookhagen, B., Coutand, I., Cowan, B., et al. (2018). Formation of a Rain Shadow: O and H stable isotope records in authigenic clays from the Siwalik Group in eastern Bhutan. *Geochemistry, Geophysics, Geosystems*, *19*(9), 3430–3447. https://doi.org/10.1029/2017GC007254

Haque, U., Da Silva, P. F., Devoli, G., Pilz, J., Zhao, B., Khaloua, A., et al. (2019). The human cost of global warming: Deadly landslides and their triggers (1995–2014). *Science of the Total Environment*, *682*, 673–684. https://doi.org/10.1016/j.scitotenv.2019.03.415

Held, I. M., & Soden, B. J. (2006). Robust responses of the hydrological cycle to global warming. *Journal of Climate*, *19*(21), 5686–5699. https://doi.org/10.1175/JCLI3990.1

Herman, F., Seward, D., Valla, P. G., Carter, A., Kohn, B., Willett, S. D., & Ehlers, T. A. (2013). Worldwide acceleration of mountain erosion under a cooling climate. *Nature*, *504*(7480), 423–426. https://doi.org/10.1038/nature12877

Huntington, T. G. (2010). Climate warming-induced intensification of the hydrologic cycle. In *Advances in agronomy* (Vol. 109, pp. 1–53). Elsevier. https://doi.org/10.1016/B978-0-12-385040-9.00001-3

Jaimes-Gutierrez, R., Adatte, T., Puceat, E., Vennemann, T., Prieur, M., Wild, A., et al. (2024). Supplementary material: "Deciphering paleocene-eocene thermal maximum climatic dynamics: Insights from oxygen and hydrogen isotopes in clay minerals of paleosols from the Southern Pyrenees" [Dataset]. In *Paleoceanography and paleoclimatology (number illuminating a warmer world: Insights from the paleogene)*. Zenodo. https://doi.org/10.5281/zenodo.10641162

Jaimes-Gutierrez, R., & Wild, A. L. (2024). Monte Carlo Python notebook, clay crystalization temperatures [Software]. *Zenodo*. https://doi.org/10.5281/zenodo.12104345

John, C. M., Banerjee, N. R., Longstaffe, F. J., Sica, C., Law, K. R., & Zachos, J. C. (2012). Clay assemblage and oxygen isotopic constraints on the weathering response to the Paleocene-Eocene thermal maximum, east coast of North America. *Geology*, *40*(7), 591–594. https://doi.org/10.1130/G32785.1

Kelson, J. R., Huntington, K. W., Breecker, D. O., Burgener, L. K., Gallagher, T. M., Hoke, G. D., & Petersen, S. V. (2020). A proxy for all seasons? A synthesis of clumped isotope data from Holocene soil carbonates. *Quaternary Science Reviews*, *234*, 106259. https://doi.org/10.1016/j.quascirev.2020.106259

Kelson, J. R., Huth, T. E., Passey, B. H., Levin, N. E., Petersen, S. V., Ballato, P., et al. (2023). Triple oxygen isotope compositions of globally distributed soil carbonates record widespread evaporation of soil waters. *Geochimica et Cosmochimica Acta*, *355*, 138–160. https://doi.org/10.1016/j.gca.2023.06.034

Kennett, J. P., & Stott, L. D. (1991). Abrupt deep-sea warming, palaeoceanographic changes and benthic extinctions at the end of the Palaeocene. *Nature*, *353*(6341), 225–229. https://doi.org/10.1038/353225a0

Khozyem, H. M. A. (2013). *Sedimentology, geochemistry and mineralogy of the Paleocene Eocene Thermal Maximum (PETM): Sediment records from Egypt, India and Spain* (Doctoral Dissertation). Université de Lausanne.

Kirtland Turner, S., Hull, P. M., Kump, L. R., & Ridgwell, A. (2017). A probabilistic assessment of the rapidity of PETM onset. *Nature Communications*, *8*(1), 353. https://doi.org/10.1038/s41467-017-00292-2

Korasidis, V. A., Wing, S. L., Shields, C. A., & Kiehl, J. T. (2022). Global changes in terrestrial vegetation and continental climate during the Paleocene-Eocene Thermal Maximum. *Paleoceanography and Paleoclimatology*, *37*(4). https://doi.org/10.1029/2021PA004325

Kraus, M. J. (1999). Paleosols in clastic sedimentary rocks: Their geologic applications. *Earth-Science Reviews*, *47*(1–2), 41–70. https://doi.org/10.1016/S0012-8252(99)00026-4

Lacroix, B., & Vennemann, T. (2015). Empirical calibration of the oxygen isotope fractionation between quartz and Fe–Mg-chlorite. *Geochimica et Cosmochimica Acta*, *149*, 21–31. https://doi.org/10.1016/j.gca.2014.10.031

Lyons, S. L., Baczynski, A. A., Babila, T. L., Bralower, T. J., Hajek, E. A., Kump, L. R., et al. (2019). Palaeocene–Eocene Thermal Maximum prolonged by fossil carbon oxidation. *Nature Geoscience*, *12*(1), 54–60. https://doi.org/10.1038/s41561-018-0277-3

Maher, K. (2010). The dependence of chemical weathering rates on fluid residence time. *Earth and Planetary Science Letters*, *294*(1–2), 101–110. https://doi.org/10.1016/j.epsl.2010.03.010

McCarthy, P. J., Martini, I. P., & Leckie, D. A. (1998). Use of micromorphology for palaeoenvironmental interpretation of complex alluvial palaeosols: An example from the Mill Creek Formation (Albian), southwestern Alberta, Canada. *Palaeogeography, Palaeoclimatology, Palaeoecology*, *143*(1–3), 87–110. https://doi.org/10.1016/S0031-0182(98)00080-7

Merseburger, S. (2022). *Stable hydrogen isotope ratios in the clay fraction of soil*. Karlsruher Instituts für Technologie.

Meunier, A. (2005). *Clays*. Springer.

Molnar, P. (2022). Differences between soil and air temperatures: Implications for geological reconstructions of past climate. *Geosphere*, *18*(2), 800–824. https://doi.org/10.1130/GES02448.1

Molnar, P., & England, P. (1990). Late Cenozoic uplift of mountain ranges and global climate change: Chicken or egg? *Nature*, *346*(6279), 29–34. https://doi.org/10.1038/346029a0

Moore, D. M., & Reynolds, R. C. (1992). *Moore, Reynolds 1997_X-Ray Diffraction.pdf (Second)*. Oxford University Press.

Muñoz, J. A. (1992). Evolution of a continental collision belt: ECORS-Pyrenees crustal balanced cross-section. In K. R. McClay (Ed.), *Thrust tectonics* (pp. 235–246). Springer Netherlands. https://doi.org/10.1007/978-94-011-3066-0_21

Myers, T. S., Tabor, N. J., Jacobs, L. L., & Mateus, O. (2012). Palaeoclimate of the Late Jurassic of Portugal: Comparison with the western United States: Late Jurassic palaeoclimate of Portugal. *Sedimentology*, *59*(6), 1695–1717. https://doi.org/10.1111/j.1365-3091.2012.01322.x

Penman, D. E., Hönisch, B., Zeebe, R. E., Thomas, E., & Zachos, J. C. (2014). Rapid and sustained surface ocean acidification during the Paleocene-Eocene Thermal Maximum. *Paleoceanography*, *29*(5), 357–369. https://doi.org/10.1002/2014PA002621

Peters, N. A., Huntington, K. W., & Hoke, G. D. (2013). Hot or not? Impact of seasonally variable soil carbonate formation on paleotemperature and O-isotope records from clumped isotope thermometry. *Earth and Planetary Science Letters*, *361*, 208–218. https://doi.org/10.1016/j.epsl.2012.10.024

Pogge von Strandmann, P. A. E., Jones, M. T., West, A. J., Murphy, M. J., Stokke, E. W., Tarbuck, G., et al. (2021). Lithium isotope evidence for enhanced weathering and erosion during the Paleocene-Eocene Thermal Maximum. *Science Advances*, *7*(42), eabh4224. https://doi.org/10.1126/sciadv.abh4224

Pratap, S., & Markonis, Y. (2022). The response of the hydrological cycle to temperature changes in recent and distant climatic history. *Progress in Earth and Planetary Science*, *9*(1), 30. https://doi.org/10.1186/s40645-022-00489-0

Prieur, M., Whittaker, A. C., Nuriel, P., Jaimes-Gutierrez, R., Garzanti, E., Roigé, M., et al. (2024). Fingerprinting enhanced floodplain reworking during the Paleocene−Eocene Thermal Maximum in the southern Pyrenees (Spain): Implications for channel dynamics and carbon burial. *Geology*, *52*(9), 651–655. https://doi.org/10.1130/G52180.1

Pujalte, V., Baceta, J. I., & Schmitz, B. (2015). A massive input of coarse-grained siliciclastics in the Pyrenean Basin during the PETM: The missing ingredient in a coeval abrupt change in hydrological regime. *Climate of the Past*, *11*(12), 1653–1672. https://doi.org/10.5194/cp-11-1653-2015

Pujalte, V., Orue-Etxebarria, X., Schmitz, B., Tosquella, J., Baceta, J. I., Payros, A., et al. (2003). In *Basal Ilerdian (earliest Eocene) turnover of larger foraminifera: Age constraints based on calcareous plankton and δ13C isotopic profiles from new southern Pyrenean sections (Spain)* (Vol. 19).

Pujalte, V., Robador, A., Payros, A., & Samsó, J. M. (2016). A siliciclastic braid delta within a lower Paleogene carbonate platform (Ordesa-Monte Perdido National Park, southern Pyrenees, Spain): Record of the Paleocene–Eocene Thermal Maximum perturbation. *Palaeogeography, Palaeoclimatology, Palaeoecology*, *459*, 453–470. https://doi.org/10.1016/j.palaeo.2016.07.029

Pujalte, V., Schmitz, B., & Baceta, J. I. (2014). Sea-level changes across the Paleocene–Eocene interval in the Spanish Pyrenees, and their possible relationship with North Atlantic magmatism. *Palaeogeography, Palaeoclimatology, Palaeoecology*, *393*, 45–60. https://doi.org/10.1016/j.palaeo.2013.10.016

Pujalte, V., Schmitz, B., Baceta, J. I., Orue-Etxebarria, X., Bernaola, G., Dinarès-Turell, J., et al. (2009). Correlation of the Thanetian-Ilerdian turnover of larger foraminifera and the Paleocene-Eocene thermal maximum: Confirming evidence from the Campo area (Pyrenees, Spain). *Geológica Acta*.

Ramos, E. J., Breecker, D. O., Barnes, J. D., Li, F., Gingerich, P. D., Loewy, S. L., et al. (2022). Swift weathering response on floodplains during the Paleocene-Eocene Thermal Maximum. *Geophysical Research Letters*, *49*(6). https://doi.org/10.1029/2021GL097436

Riebe, C. S., Kirchner, J. W., & Finkel, R. C. (2004). Erosional and climatic effects on long-term chemical weathering rates in granitic landscapes spanning diverse climate regimes. *Earth and Planetary Science Letters*, *224*(3–4), 547–562. https://doi.org/10.1016/j.epsl.2004.05.019

Robert, C., & Kennett, J. P. (1992). In *Paleocene and Eocene kaolinite distribution in the South Atlantic and Southern Ocean: Antarctic climatic and paleoceanographic implications* (Vol. 103, pp. 99–110).

Röhl, U., Westerhold, T., Bralower, T. J., & Zachos, J. C. (2007). On the duration of the Paleocene-Eocene thermal maximum (PETM). *Geochemistry, Geophysics, Geosystems*, *8*(12), 2007GC001784. https://doi.org/10.1029/2007GC001784

Rosenau, N. A., & Tabor, N. J. (2013). Oxygen and hydrogen isotope compositions of paleosol phyllosilicates: Differential burial histories and determination of Middle–Late Pennsylvanian low-latitude terrestrial paleotemperatures. *Palaeogeography, Palaeoclimatology, Palaeoecology*, *392*, 382–397. https://doi.org/10.1016/j.palaeo.2013.09.020

Rosenbaum, G., Lister, G. S., & Duboz, C. (2002). Relative motions of Africa, Iberia and Europe during Alpine orogeny. *Tectonophysics*, *359*(1–2), 117–129. https://doi.org/10.1016/S0040-1951(02)00442-0

Roure, F., Choukroune, P., Berastegui, X., Munoz, J. A., Villien, A., Matheron, P., et al. (1989). Ecors deep seismic data and balanced cross sections: Geometric constraints on the evolution of the Pyrenees. *Tectonics*, *8*(1), 41–50. https://doi.org/10.1029/TC008i001p00041

Rush, W. D., Kiehl, J. T., Shields, C. A., & Zachos, J. C. (2021). Increased frequency of extreme precipitation events in the North Atlantic during the PETM: Observations and theory. *Palaeogeography, Palaeoclimatology, Palaeoecology*, *568*, 110289. https://doi.org/10.1016/j.palaeo.2021.110289

Savin, S. M., & Epstein, S. (1970). The oxygen and hydrogen isotope geochemistry of clay minerals. *Geochimica et Cosmochimica Acta*, *34*(1), 25–42. https://doi.org/10.1016/0016-7037(70)90149-3

Schmitz, B., & Pujalte, V. (2003). Sea-level, humidity, and land-erosion records across the initial Eocene thermal maximum from a continental-marine transect in northern Spain. *Geology*, *31*(8), 689. https://doi.org/10.1130/G19527.1

Schmitz, B., & Pujalte, V. (2007). Abrupt increase in seasonal extreme precipitation at the Paleocene-Eocene boundary. *Geology*, *35*(3), 215. https://doi.org/10.1130/G23261A.1

Schmitz, B., Pujalte, V., & Nunhez-Betelu, K. (2001). Climate and sea-level perturbations during the Initial Eocene Thermal Maximum: Evidence from siliciclastic units in the Basque Basin (Ermua, Zumaia and Trabakua Pass), northern Spain. *Palaeogeography, Palaeoclimatology, Palaeoecology*, *165*, 299–320.

Sharp, Z. D. (1990). A laser-based microanalytical method for the in situ determination of oxygen isotope ratios of silicates and oxides. *Geochimica et Cosmochimica Acta*, *54*(5), 1353–1357. https://doi.org/10.1016/0016-7037(90)90160-M

Sheldon, N. D., & Tabor, N. J. (2009). Quantitative paleoenvironmental and paleoclimatic reconstruction using paleosols. *Earth-Science Reviews*, *95*(1–2), 1–52. https://doi.org/10.1016/j.earscirev.2009.03.004

Sheppard, S. M. F., & Gilg, H. A. (1996). In *Stable isotope geochemistry of clay minerals* (Vol. 31, pp. 1–24).

Shields, C. A., Kiehl, J. T., Rush, W., Rothstein, M., & Snyder, M. A. (2021). Atmospheric rivers in high-resolution simulations of the Paleocene Eocene Thermal Maximum (PETM). *Palaeogeography, Palaeoclimatology, Palaeoecology*, *567*, 110293. https://doi.org/10.1016/j.palaeo.2021.110293

Soil Survey Staff. (1999). Soil taxonomy: A basic system of soil classification for making and interpreting soil surveys. In *United States deptartment of agriculture natural resources conservation service* (2nd ed.).

Soil Survey Staff. (2022). *Keys to soil taxonomy* (13th ed.). United States Department of Agriculture Natural Resources Conservation Service.

Tabor, N. J., Montañez, I. P., Scotese, C. R., Poulsen, C. J., & Mack, G. H. (2008). Paleosol archives of environmental and climatic history in paleotropical western Pangea during the latest Pennsylvanian through Early Permian. In *Special Paper 441: Resolving the Late Paleozoic Ice Age in Time and Space* (Vol. 441, pp. 291–303). Geological Society of America. https://doi.org/10.1130/2008.2441(20)

Tabor, N. J., & Myers, T. S. (2015). Paleosols as indicators of paleoenvironment and paleoclimate. *Annual Review of Earth and Planetary Sciences*, *43*(1), 333–361. https://doi.org/10.1146/annurev-earth-060614-105355

Tabor, N. J., Myers, T. S., Gulbranson, E., Rasmussen, C., & Sheldon, N. D. (2013). Carbon stable isotope composition of modern calcareous soil profiles in California: Implications for CO_2 reconstructions from calcareous paleosols. In L. C. Nordt & S. G. Driese (Eds.), *New frontiers in paleopedology and terrestrial paleoclimatology: Paleosols and soil surface analog systems* (pp. 17–34). SEPM (Society for Sedimentary Geology). https://doi.org/10.2110/sepmsp.104.07

Thiry, M. (2000). Palaeoclimatic interpretation of clay minerals in marine deposits: An outlook from the continental origin. *Earth-Science Reviews*, *49*(1–4), 201Â–221. https://doi.org/10.1016/S0012-8252(99)00054-9

Thomas, E., & Shackleton, N. J. (1996). The Paleocene-Eocene benthic foraminiferal extinction and stable isotope anomalies. *Geological Society, London, Special Publications*, *101*(1), 401–441. https://doi.org/10.1144/GSL.SP.1996.101.01.20

Tremblin, M., Khozyem, H., Adatte, T., Spangenberg, J. E., Fillon, C., Grauls, A., et al. (2022). Mercury enrichments of the Pyrenean foreland basins sediments support enhanced volcanism during the Paleocene-Eocene thermal maximum (PETM). *Global and Planetary Change*, *212*, 103794. https://doi.org/10.1016/j.gloplacha.2022.103794

Trenberth, K. E., Dai, A., Rasmussen, R. M., & Parsons, D. B. (2003). The changing character of precipitation. *Bulletin of the American Meteorological Society*, *84*(9), 1205–1218. https://doi.org/10.1175/BAMS-84-9-1205

Velde, B., & Meunier, A. (2008). *The origin of clay minerals in soils and weathered rocks*. Springer Berlin Heidelberg. https://doi.org/10.1007/978-3-540-75634-7

Vimpere, L., Spangenberg, J. E., Roige, M., Adatte, T., De Kaenel, E., Fildani, A., et al. (2023). Carbon isotope and biostratigraphic evidence for an expanded Paleocene–Eocene Thermal Maximum sedimentary record in the deep Gulf of Mexico. *Geology*, *51*(4), 334–339. https://doi.org/10.1130/G50641.1

Voigt, W., & Freyer, D. (2023). Solubility of anhydrite and gypsum at temperatures below 100°C and the gypsum-anhydrite transition temperature in aqueous solutions: A re-assessment. *Frontiers in Nuclear Engineering*, *2*, 1208582. https://doi.org/10.3389/fnuen.2023.1208582

Watson, A. (1992). Chapter 10—Desert soils. In *Developments in Earth surface processes* (Vol. 2, pp. 225–260). Elsevier. https://doi.org/10.1016/b978-0-444-89198-3.50015-5

West, A., Galy, A., & Bickle, M. (2005). Tectonic and climatic controls on silicate weathering. *Earth and Planetary Science Letters*, *235*(1–2), 211–228. https://doi.org/10.1016/j.epsl.2005.03.020

Westerhold, T., Röhl, U., Frederichs, T., Agnini, C., Raffi, I., Zachos, J. C., & Wilkens, R. H. (2017). Astronomical calibration of the Ypresian timescale: Implications for seafloor spreading rates and the chaotic behavior of the solar system? *Climate of the Past*, *13*(9), 1129–1152. https://doi.org/10.5194/cp-13-1129-2017

Westerhold, T., Röhl, U., McCarren, H. K., & Zachos, J. C. (2009). Latest on the absolute age of the Paleocene–Eocene Thermal Maximum (PETM): New insights from exact stratigraphic position of key ash layers +19 and −17. *Earth and Planetary Science Letters*, *287*(3–4), 412–419. https://doi.org/10.1016/j.epsl.2009.08.027

Wing, S. L., & Currano, E. D. (2013). Plant response to a global greenhouse event 56 million years ago. *American Journal of Botany*, *100*(7), 1234–1254. https://doi.org/10.3732/ajb.1200554

Wright, J. D., & Schaller, M. F. (2013). Evidence for a rapid release of carbon at the Paleocene-Eocene thermal maximum. *Proceedings of the National Academy of Sciences of the United States of America*, *110*(40), 15908–15913. https://doi.org/10.1073/pnas.1309188110

Yeh, H. W. (1979). D/H Ratios and late-stage dehydration of shales during burial. *Geochimica et Cosmochimica Acta*, *44*, 341Â–352.

Zachos, J. C., Röhl, U., Schellenberg, S. A., Sluijs, A., Hodell, D. A., Kelly, D. C., et al. (2005). Rapid acidification of the ocean during the Paleocene-Eocene Thermal Maximum. *Science*, *308*(5728), 1611–1615. https://doi.org/10.1126/science.1109004

Zachos, J. C., Wara, M. W., Bohaty, S., Delaney, M. L., Petrizzo, M. R., Brill, A., et al. (2003). A transient rise in tropical sea surface temperature during the Paleocene-Eocene Thermal Maximum. *Science*, *302*(5650), 1551–1554. https://doi.org/10.1126/science.1090110

Zeebe, R. E., & Lourens, L. J. (2019). Solar System chaos and the Paleocene–Eocene boundary age constrained by geology and astronomy. *Science*, *365*(6456), 926–929. https://doi.org/10.1126/science.aax0612